Journal of Computational Physics **165,** 1–21 (2000)
doi:10.1006/jcph.2000.6583, available online at http://www.idealibrary.com on IDEAL®

Fast Calculations of Dyadic Green's Functions for Electromagnetic Scattering in a Multilayered Medium

Wei Cai and Tiejun Yu

Department of Mathematics, University of North Carolina at Charlotte, Charlotte, North Carolina 28223
E-mail: wcai@uncc.edu

Received November 15, 1999; revised April 28, 2000; published online November 3, 2000

In this paper, we introduce a novel acceleration method for the calculation of dyadic Green's functions for the mixed potential integral equation formulation of electromagnetic scattering of scatterers embedded in a multilayered medium. Numerical results are provided to demonstrate the efficiency and accuracy of the proposed method.

Key Words: electromagnetic scattering; dyadic Green's functions; mixed potential integral equations; Hankel transforms; fast algorithms; window functions.

1. INTRODUCTION

Integral equation formulation of electromagnetic scattering of conductive surfaces is a popular approach for many applications, including the parametric extraction for IC interconnects and computer packaging simulations [1] and the performance of multilayered antenna calculations [2]. The main advantage of the integral formulation [2, 3] is reduction of unknowns and its flexibility in handling very complex geometries of the scattering surface and the automatic enforcement of Sommerfeld exterior decaying conditions by the construction of proper Green's functions in the multilayered medium usually encountered in those applications [4].

However, the calculation of the dyadic Green's functions in a multilayered medium has been one of the bottlenecks in the effort to increase the speed of integral equation methods; the other major bottleneck has been the solution of the impedance matrix resulting from the boundary element methods or method of moments [2]. Extensive research has been done on accelerating the calculation speed of the dyadic Green's functions in a multilayered medium [3, 5–7]. The key difficulty is the calculation of the Sommerfeld integral appearing in the Hankel transformation, which defines the time domain dyadic Green's functions in terms of their Fourier spectral forms. Such difficulty comes from several factors: (a) the existence

0021-9991/00 $35.00

of surface wave poles in the spectral form of the Green's functions [3], which affects the selection of the contour path in the Sommerfeld integral; (b) the slow decay of the spectral Green's functions, especially when the field location and source location are close, as in many of the VLSI and MMIC applications; and (c) the oscillatory behavior of the Hankel transformation kernel (i.e., $J_0(z)$) and the highly oscillatory profile of the spectral Green's functions in a complex integration contour.

Several methods have been proposed to address the difficulties mentioned above. For example, the Prony type method originally proposed in [5], and later modified in [6], tries to extract the surface wave poles from the spectral form of the Green's function; then exponential functions are used to approximate the remaining part of the Green's function in the spectral domain. The main problem with this approach is the requirement of pole extraction. Techniques to extract the pole have been found to be very unstable and pole extraction is close to impossible when many layers are considered. Also, approximation of spectral Green's functions by exponentials via a Prony technique is not efficient for high-frequency problems or when the source and observation points are not on the same layer in a multilayered structure. Another approach [7] is to try to find a steep descent path for the Sommerfeld integration, which again is not easy for many layered media.

In this paper, we present a novel method which utilizes a window function as a convolution kernel to the time domain Green's function. The effect of this window function is to modulate the decay of the integrand in the Sommerfeld integration. The idea of convolution with a window function in the time domain is equivalent to a low-pass filter in the frequency domain used in signal processing and Gabor transformation in wavelet theory [8]. A similar approach has been used to recover high-order approximations of discontinuous functions from their Fourier coefficients in spectral methods [9]. The fast decay rate of the window function in the spectral domain effectively creates a steep descent path for the integration without the existence or the information of the location of possible steep descent paths for the spectral Green's functions. Extensive numerical results have confirmed the effectiveness of this method, especially when the observation and source locations are close, whereas the Sommerfeld integration will converge extremely slow. A comprehensive code WDS (Wave Design Simulator) [10], which uses this window function technique, has been used to carry out 3-D full wave analysis of RF components and scattering of general objects in arbitrary multilayered media.

The rest of the paper is divided into the following sections: Section 2 gives a brief introduction to the dyadic Green's functions in a multilayered medium; in Section 3, Green's functions for the vector and scalar potentials used in the mixed potential integral equations are described; Section 4 gives the window-function-based acceleration technique and error estimations; Section 5 provides several numerical examples to demonstrate the effectiveness and accuracy of the proposed methods; and a conclusion is given in Section 6. The appendix contains technique derivations and proofs.

2. DYADIC GREEN'S FUNCTION IN MULTILAYERED MEDIA

In this section we present the setup for the dyadic Green's functions $\bar{\mathbf{G}}_E(\mathbf{r} \mid \mathbf{r}')$, $\bar{\mathbf{G}}_H(\mathbf{r} \mid \mathbf{r}')$ in a multilayered medium. As we only consider time-harmonic fields, a time-harmonic factor $e^{j\omega t}$ is assumed in all field quantities. The medium considered is shown in Fig. 1. It is a stratified structure consisting of $N+1$ dielectric layers separated by N planar interfaces parallel to the x–y plane of a Cartesian coordinate system and located at $z = -d_i$, $i = 0, 1, \ldots, N$.

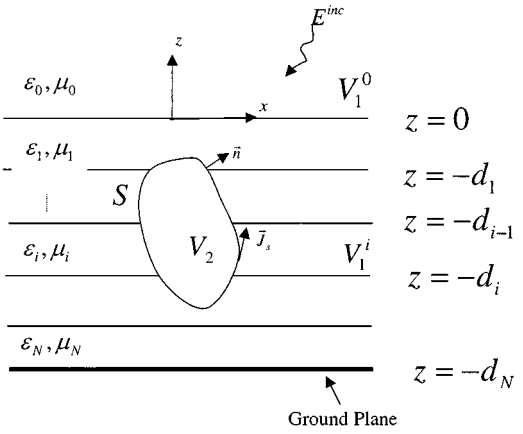

FIG. 1. A three-dimensional scatterer embedded in an $N + 1$ layered medium.

The medium of the mth layer is characterized by permeability μ_m and permittivity ε_m. Components of dyadic Green's functions $\bar{\mathbf{G}}_E(\mathbf{r} \mid \mathbf{r}')$, $\bar{\mathbf{G}}_H(\mathbf{r} \mid \mathbf{r}')$ represent the electromagnetic fields at location $\mathbf{r}$ excited by current Hertz dipole at $\mathbf{r}'$; namely, G_E^{st} is the s-component of the electric field generated by a t-oriented current Hertz dipole, $s, t = x, y, z$.

2.1. *Two-Dimensional Fourier and Hankel Transformations*

As the multilayered medium is radially symmetric in the x–y plane, we can apply the two-dimensional Fourier transform to the Maxwell equations [11] to obtain the components of the dyadic Green's function in the Fourier transform (spectral) domain. The following identities will be used in finding the Green's function in time domain once the spectral form of the Green's function is obtained:

$$\mathcal{F}\{f(x, y)\} = \tilde{f}(k_x, k_y) = \frac{1}{2\pi} \int_{-\infty}^{\infty} \int_{-\infty}^{\infty} f(x, y) e^{-j[k_x x + k_y y]}\, dx\, dy \tag{2.1}$$

$$\mathcal{F}^{-1}\{\tilde{f}(k_x, k_y)\} = f(x, y) = \frac{1}{2\pi} \int_{-\infty}^{\infty} \int_{-\infty}^{\infty} \tilde{f}(k_x, k_y) e^{j[k_x x + k_y y]}\, dk_x\, dk_y. \tag{2.2}$$

The Fourier integrals (2.1)–(2.2) can be conveniently expressed in terms of the Hankel transform if $f(x, y) = f(\rho)$ is a radially symmetric function of ρ. Introducing polar coordinates in both the transform and space domains,

$$x = \rho \cos\beta, \quad y = \rho \sin\beta,$$
$$k_x = k_\rho \cos\alpha, \quad k_y = k_\rho \sin\alpha,$$

where

$$\rho = \sqrt{x^2 + y^2}, \quad \beta = \arctan\left(\frac{y}{x}\right),$$
$$k_\rho = \sqrt{k_x^2 + k_y^2}, \quad \alpha = \arctan\left(\frac{k_y}{k_x}\right),$$

we can show that

$$\tilde{f}(k_\rho) = \mathcal{F}\{f(\rho)\} = S_0[f(\rho)](k_\rho) \tag{2.3}$$

and

$$f(\rho) = \mathcal{F}^{-1}\{\tilde{f}(k_\rho)\} = S_0[\tilde{f}(k_\rho)](\rho), \tag{2.4}$$

where the nth-order Hankel transform $S_n[\tilde{f}(k_\rho)]$ for integer $n \geq 0$, is defined as

$$S_n[\tilde{f}(k_\rho)](\rho) = \int_0^\infty \tilde{f}(k_\rho) J_n(k_\rho \rho) k_\rho^{n+1}\, dk_\rho \tag{2.5}$$

and the roles of ρ and k_ρ can be switched and where $J_n(z)$ is the nth-order Bessel function.

2.2. *Dyadic Green's Functions* $\bar{\mathbf{G}}_E, \bar{\mathbf{G}}_H$

From the Maxwell equations [11], the electric field is shown to satisfy the vector equation

$$\boldsymbol{\nabla} \times \boldsymbol{\nabla} \times \mathbf{E} - k^2 \mathbf{E} = -j\omega\mu\, \mathbf{J} \tag{2.6}$$

where $\mathbf{J}$ is the current source. In a source-free region, we have the following vector Helmholtz equation:

$$\boldsymbol{\nabla}^2 \mathbf{E} + k^2 \mathbf{E} = j\omega\mu\, \mathbf{J}. \tag{2.7}$$

The dyadic electric Green's function $\bar{\mathbf{G}}_E^{:t}$ is the solution to (2.7) when the source is a t-directed electric dipole, namely $\mathbf{J}(r) = \frac{1}{j\omega\mu}\delta(\mathbf{r} - \mathbf{r}')t$. The magnetic dyadic Green's function $\bar{\mathbf{G}}_H$ can be obtained by

$$\bar{\mathbf{G}}_H(\mathbf{r} \mid \mathbf{r}') = -\frac{1}{j\omega\mu} \boldsymbol{\nabla} \times \bar{\mathbf{G}}_E(\mathbf{r} \mid \mathbf{r}'). \tag{2.8}$$

3. DYADIC GREEN'S FUNCTIONS $\bar{\mathbf{G}}_A(\mathbf{r} \mid \mathbf{r}')$, $G_V(\mathbf{r} \mid \mathbf{r}')$

In this section, we describe the dyadic Green's functions for both vector potentials and scalar potentials. These are used for the mixed potential integral equation formulation (MPIE) of scattering problems [3, 4].

In a MPIE formulation, the electromagnetic fields can be expressed in terms of a vector potential $\mathbf{A}$ and a scalar potential V_e, i.e.,

$$\mathbf{E} = -j\omega\, \mathbf{A} - \boldsymbol{\nabla} V_\mathrm{e} \tag{3.1}$$

$$\mathbf{H} = \frac{1}{\mu} \boldsymbol{\nabla} \times \mathbf{A}, \tag{3.2}$$

where

$$\boldsymbol{\nabla}^2 \mathbf{A} + k^2 \mathbf{A} - \mu \boldsymbol{\nabla} \frac{1}{\mu} \times \boldsymbol{\nabla} \times \mathbf{A} = -\mu\, \mathbf{J}_\mathrm{e} \tag{3.3}$$

and where $\mathbf{J}_e$ is the electric current source and $k^2 = \omega^2\epsilon\mu$. Equation (3.3) simplifies to the following equation when μ is a constant:

$$\nabla^2\mathbf{A} + k^2\mathbf{A} = -\mu\,\mathbf{J}_e. \tag{3.4}$$

If the Lorentz gauge condition is used to relate V_e to $\mathbf{A}$, i.e.,

$$\nabla\cdot\mathbf{A} = -j\omega\epsilon\mu V_e, \tag{3.5}$$

then we have

$$\nabla^2 V_e + k^2 V_e = -\frac{1}{\epsilon}\rho_e, \tag{3.6}$$

where ρ_e is the charge density related to the electric current $\mathbf{J}_e$ by the continuity equation

$$\nabla\cdot\mathbf{J}_e + j\omega\rho_e = 0. \tag{3.7}$$

The vector potentials used to represent the magnetic field $\mathbf{H}$ in (3.2) are not unique and there are many ways of defining the potentials. Two of the most used approaches are Sommerfeld potentials [12] and transverse potentials [13, 14]. In formulating these potentials, we take into account that only two components of the magnetic field are independent, thus only two components of these vector potentials are sufficient. In the Sommerfeld potential formulation, it is stipulated that the electromagnetic fields from a horizontal electric dipole (HED) can be represented by a horizontal component of $\mathbf{A}$ in the same direction of the HED and the z-component of $\mathbf{A}$; fields of a VED (vertical electric dipole) will be represented by only the z-component of $\mathbf{A}$. In contrast, for the transverse potential formulation, HED generated electromagnetic fields will be represented by two transverse components of $\mathbf{A}$ while a VED generated field is represented by only the z-component of $\mathbf{A}$. Other potentials include Hertz–Debye potentials [15].

Sommerfeld potential. The dyadic Green's function $\bar{\mathbf{G}}_A$ for the Sommerfeld vector potential $\mathbf{A}$ [12] has the form

$$\bar{\mathbf{G}}_A = \left(\hat{x}G_A^{xx} + \hat{z}G_A^{zx}\right)\hat{x} + \left(\hat{y}G_A^{yy} + \hat{z}G_A^{zy}\right)\hat{y} + \hat{z}G_A^{zz}\hat{z}. \tag{3.8}$$

Transverse potentials. The dyadic Green's function $\bar{\mathbf{G}}_A$ for the transverse vector potential $\mathbf{A}$ [13, 14] has the form

$$\bar{\mathbf{G}}_A = \left(\hat{x}G_A^{xx} + \hat{y}G_A^{yx}\right)\hat{x} + \left(\hat{x}G_A^{xy} + \hat{y}G_A^{yy}\right)\hat{y} + \hat{z}G_A^{zz}\hat{z}. \tag{3.9}$$

The scalar potential $G_V(\mathbf{r}\mid\mathbf{r}')$ and the components in the Sommerfeld and transverse potentials can be obtained in the spectral domain; explicit formulas can be found in [3, 10].

4. FAST CALCULATION OF DYADIC GREEN'S FUNCTIONS $\bar{\mathbf{G}}_A(\rho, z; z')$, $\mathbf{G}_V(\rho, z; z')$

The spectral components of the vector and scalar potential Green's function $\tilde{G}_A(\rho, z; z')$ and $\tilde{G}_V(k_\rho, z; z')$ in Section 3 can be shown [3, 10] to consist of terms such as

$$jk_x\tilde{G}(k_\rho, z; z'), \quad jk_y\tilde{G}(k_\rho, z; z') \tag{4.1}$$

where $\tilde{G}(k_\rho, z; z')$ is a function of k_ρ. Thus, the inverse Fourier transform of (4.1) can be evaluated as

$$\mathcal{F}^{-1}\{jk_x\tilde{G}(k_\rho, z; z')\} = \frac{\partial}{\partial x}\mathcal{F}^{-1}\{\tilde{G}(k_\rho, z; z')\} = \frac{\partial}{\partial x}S_0(\tilde{G}(k_\rho, z; z')) \tag{4.2}$$

$$\mathcal{F}^{-1}\{jk_y\tilde{G}(k_\rho, z; z')\} = \frac{\partial}{\partial y}\mathcal{F}^{-1}\{\tilde{G}(k_\rho, z; z')\} = \frac{\partial}{\partial y}S_0(\tilde{G}(k_\rho, z; z')). \tag{4.3}$$

The partial derivatives with respect to x or y can be approximated by a finite difference formula with appropriate accuracy. Therefore, we only have to discuss an acceleration algorithm for calculating the Hankel transformation

$$G(\rho, z; z') = S_0(\tilde{G}(k_\rho, z; z')) = \int_C \tilde{G}(k_\rho, z; z')\, J_0(\rho k_\rho) k_\rho \, dk_\rho, \tag{4.4}$$

where the contour C should be in the first quadrant of the complex wavenumber k_ρ space from 0 to ∞.

The main difficulty involving the calculation of function $G(\rho, z; z')$ via the Hankel transform (4.4) is the fact that the integrand decays very slowly when $z = z'$, or $z \sim z'$ (i.e., when the source point and the observation point are on or nearly on the same horizontal plane). In order to accelerate the calculation of $G(\rho, z; z')$ when $z \sim z'$ or $z = z'$, we introduce the following mth-order window function $\psi_a(x, y) = \psi_a(\rho)$ with a support size a:

$$\psi_a(\rho) = \begin{cases} \left(1 - \left(\frac{\rho}{a}\right)^2\right)^m, & \text{if } \rho \le a \\ 0, & \text{otherwise.} \end{cases} \tag{4.5}$$

We have the following lemma regarding the window function $\psi_a(\rho)$.

LEMMA 1. *For any cylindrical symmetrical function $f(\rho)$, we have the identity*

$$f(x, y) * \psi_a(x, y) = S_0[\tilde{f}(k_\rho)\tilde{\psi}_a(k_\rho)](\rho), \tag{4.6}$$

where

$$\tilde{f}(k_\rho) = S_0[f(\rho)](k_\rho)$$

and

$$\tilde{\psi}_a(k_\rho) = S_0[\psi_a(\rho)](k_\rho).$$

To recover the value of $f(x, y)$ from its Hankel transform, we also need the following result.

LEMMA 2. *Let $f(x, y)$ be a C^2 function. Then it can be shown that*

$$f(x, y) * \psi_a(x, y) = M_0 f(x, y) + M_2(f_{xx}(\xi, 0) + f_{yy}(\xi, 0)), \tag{4.7}$$

where $0 \le \xi \le \rho = \sqrt{x^2 + y^2}$ and

$$M_0 = \int_{\sqrt{x^2+y^2} \le a} \psi_a(x, y)\, dx\, dy = \frac{\pi a^2}{m+1}$$

$$M_2 = \int_{\sqrt{x^2+y^2} \le a} \psi_a(x, y) x^2\, dx\, dy.$$

Proof. The estimate (4.7) can be obtained by using a second-order Taylor expansion for the function $f(x', y')$ at point (x, y) and using the fact that terms such as $(x' - x)$ and $(y' - y)$ will vanish in the convolution with the radial symmetrical function $\psi_a(x, y)$. ■

As a result of (4.6) and (4.7), we can approximate $f(x, y)$ as

$$f(x, y) = \frac{1}{M_0} S_0[\tilde{f}(k_\rho)\tilde{\psi}_a(k_\rho)](\rho) + O(a^2) \quad \text{as } a \to 0. \tag{4.8}$$

Applying (4.8) to $G(\rho, z'; z')$, we obtain the following algorithm.

ALGORITHM 1 (Fast algorithm for $G(\rho, z; z')$). For $\rho > a$,

$$G(\rho, z; z') = \frac{1}{M_0} W_0(\rho) + O(a^2) \quad \text{as } a \to 0, \tag{4.9}$$

where

$$W_0(\rho) = S_0[\tilde{G}(k_\rho, z; z')\tilde{\psi}_a(k_\rho)](\rho). \tag{4.10}$$

Remark 1. Algorithm 1 requires condition $\rho > a$ as otherwise the Green's function will be unsmooth and the estimate in (4.7) will not be valid.

Therefore, to apply the approximation (4.8) to function $G(\rho, z'; z')$ for $\rho \le a$, we will rewrite $G(\rho, z'; z')$ as

$$G(\rho, z; z') = G_2(\rho, z; z')/r^2, \tag{4.11}$$

where $r = \sqrt{x^2 + y^2 + (z - z')^2}$. From the singularity property of the vector and scalar potential Green's function [16], we can assume that $G_2(\rho, z; z') = r^2 G(\rho, z; z')$ is a smooth function, and the approximation (4.8) thus can be used. Meanwhile, we have the following identity.

LEMMA 3. *Let* $G_2(\rho, z; z') = r^2 G(\rho, z; z')$, *with* $r = \sqrt{\rho^2 + (z - z')^2}$. *Then*

$$G_2(\rho, z; z') * \psi_a(x, y) = r^2 W_0(\rho) - 2\rho W_1(\rho) + W_2(\rho), \tag{4.12}$$

where

$$W_1(\rho) = S_0[\tilde{G}(k_\rho, z; z')\tilde{\psi}_a^*(k_\rho)](\rho) \tag{4.13}$$

$$W_2(\rho) = S_0[\tilde{G}(k_\rho, z; z')\tilde{\psi}_a^{**}(k_\rho)](\rho) \tag{4.14}$$

and

$$\tilde{\psi}_a(k_\rho) = S_0[\psi_a(\rho)](k_\rho) = \int_0^a \psi_a(\rho) J_0(k_\rho \rho)\rho \, d\rho \tag{4.15}$$

$$\tilde{\psi}_a^*(k_\rho) = S_1[\psi_a(\rho)](k_\rho) = \int_0^a \psi_a(\rho) J_1(k_\rho \rho)\rho^2 \, d\rho \tag{4.16}$$

$$\tilde{\psi}_a^{**}(k_\rho) = \int_0^a \psi_a(\rho) J_0\left(k_\rho \rho\right) \rho^3 \, d\rho. \tag{4.17}$$

Proof. The proof of (4.12) can be found in the Appendix. ■

Combining (4.7) and (4.12), we have the following approximation scheme to the Green's function.

ALGORITHM 2 (Fast Algorithm for $G(\rho, z; z')$). If $\rho > 0, a \to 0$, then

$$G(\rho, z; z') = \frac{1}{M_0 r^2}[r^2 W_0(\rho) - 2\rho W_1(\rho) + W_2(\rho)] + O(a^2). \tag{4.18}$$

Next, we will address the issue of how to calculate $W_0(\rho)$, $W_1(\rho)$, and $W_2(\rho)$. First we need the following spectral properties of $\psi_a(\rho)$ and $\tilde{\psi}_a^*(k_\rho)$ and $\tilde{\psi}_a^{**}(k_\rho)$.

LEMMA 4. *The Hankel transform $\tilde{\psi}_a(k_\rho)$ for $\psi_a(\rho)$ and $\tilde{\psi}_a^*(k_\rho)$ and $\tilde{\psi}_a^{**}(k_\rho)$ have the following decaying properties, i.e., as $|k_\rho| \to \infty$:*

$$|\tilde{\psi}_a(k_\rho)| = o(|ak_\rho|^{-m}) \tag{4.19}$$

$$|\tilde{\psi}_a^*(k_\rho)| = o(|ak_\rho|^{-m+1}) \tag{4.20}$$

$$|\tilde{\psi}_a^{**}(k_\rho)| = o(|ak_\rho|^{-m}). \tag{4.21}$$

Proof. We will outline the proof of (4.19), the other two decay conditions can be shown similarly. Using the equivalence between the 2-D Fourier transform and the Hankel transform (2.3), we can rewrite $\tilde{\psi}_a(k_\rho)$ as

$$\tilde{\psi}_a(k_\rho) = \mathcal{F}(\psi_a)(k_\rho, 0) = \frac{1}{2\pi} \int_{-\infty}^{\infty} \int \psi_a(x, y) e^{-jk_\rho x}\, dx\, dy$$

which, after integration by parts with respect to x variable m times, becomes

$$\tilde{\psi}_a(k_\rho) = \frac{(-1)^m}{2\pi(-jk_\rho)^m} \int_{-\infty}^{\infty} \int \frac{\partial^m \psi_a}{\partial^m x}(x, y) e^{-jk_\rho x}\, dx\, dy = o\left(\frac{1}{k_\rho^m}\right).$$

To derive the estimate (4.20) for $\tilde{\psi}_a^*(k_\rho)$, we first use the identity $J_0'(x) = -J_1(x)$ and integrate by parts with respect to ρ to rewrite $\psi_a^*(k_\rho)$ as

$$\tilde{\psi}_a^*(k_\rho) = \int_0^a \phi(\rho) J_0(k_\rho \rho) \rho\, d\rho$$

where $\phi(\rho) = \psi_a'(\rho)\rho + 2\psi_a(\rho)$. Then, the same proof can be used to get (4.20). ■

The fast decay condition of (4.19)–(4.21) ensures that a short integration contour can be selected without sacrificing the accuracy of approximation of Algorithms 1 and 2.

4.1. *Selection of Contour C and Window Order m and Support a*

It is well known that the spectral form $\tilde{G}(k_\rho, z; z')$ has surface wave poles which are located in the fourth quadrant of the complex k_ρ plane. Therefore, we should deform the integration contour in the definition of $W_i(\rho)$, $i = 0, 1, 2$, to a complex contour which stays away from the surface poles. A simple contour C, suggested in Fig. 2, consists of four

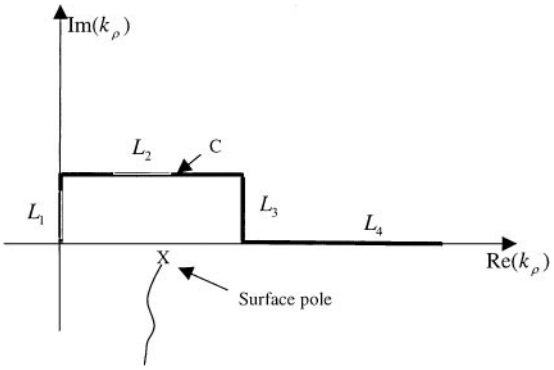

FIG. 2. Contour C for Algorithms 1 and 2.

straight segments L_i, $1 \le i \le 4$. The last segment L_4 will be finite and is determined by the decay properties of (4.19)–(4.21).

To maintain the second-order accuracy $O(a^2)$ of Algorithms 1 and 2, we will choose the L_4 portion of the contour C in Fig. 2 to satisfy the following minimum condition, while using the decay condition (4.19)–(4.21):

$$L_4 \ge \left[\frac{C_\infty}{a^2(m-s-3)}\right]^{\frac{1}{m-s-3}}. \tag{4.22}$$

Here we assume that for $k_\rho \in [k_{\max}, \infty)$, we have for some integer s and constant C_∞

$$|\tilde{G}(k_\rho, z; z')| \le C_\infty (k_\rho)^s.$$

The window support a is the primary parameter to consider. It is determined by the second-order accuracy estimate (4.18) for the algorithm for the dyadic Green's function. Once a is selected, the length of the contour L_4 should be given by (4.22).

The order of the window function m in principle should be large to have faster decays of $\tilde{\psi}_a(k_\rho)$, $\tilde{\psi}_a^*(k_\rho)$, and $\tilde{\psi}_a^{**}(k_\rho)$ according to (4.19)–(4.21). However, for smaller value of k_ρ, windows with lower order may have smaller magnitude in the spectral domain (see Figs. 3–5). In our numerical tests, a window $\psi_a(\rho)$ of order 5 ($m = 5$) was a good overall choice.

4.2. *Calculations of $\tilde{\psi}_a(k_\rho)$, $\tilde{\psi}_a^*(k_\rho)$, and $\tilde{\psi}_a^{**}(k_\rho)$*

In practice, these functions can be precalculated for a range of k_ρ as determined by the estimate (4.22). For small argument, they can be calculated directly by Gauss quadratures, while for larger k_ρ we can use the identities

$$\tilde{\psi}_a(k_\rho) = \sum_{i=0}^{m} C_i^m (-1)^i \frac{1}{a^{2i} k_\rho^{2i+2}} I_{2i+1}^0(ak_\rho)$$

$$\tilde{\psi}_a^*(k_\rho) = \sum_{i=0}^{m} C_i^m (-1)^i \frac{1}{a^{2i} k_\rho^{2i+3}} I_{2i+2}^1(ak_\rho)$$

$$\tilde{\psi}_a^{**}(k_\rho) = \sum_{i=0}^{m} C_i^m (-1)^i \frac{1}{a^{2i} k_\rho^{2i+4}} I_{2i+3}^0(ak_\rho),$$

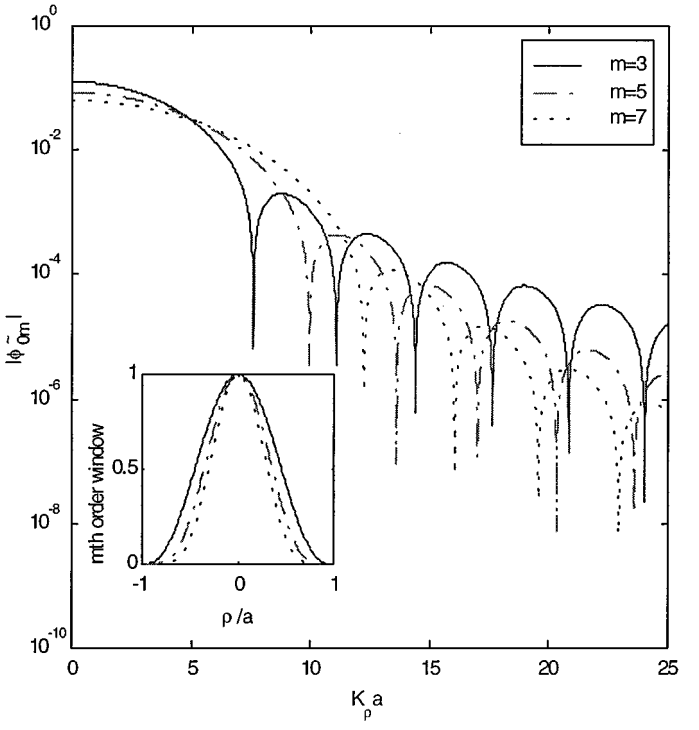

FIG. 3. The spectral decay of window functions $\tilde{\psi}_a(k_\rho)$, $a = 1$ of order $m = 3, 5, 7$. Inset is the shape of window function $\psi_a(\rho)$, $a = 1$ of order $m = 3, 5, 7$.

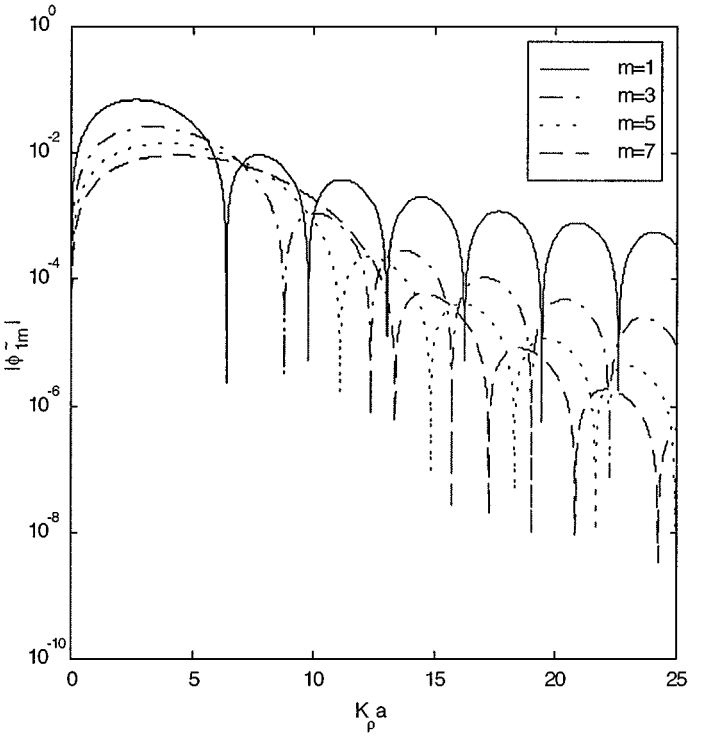

FIG. 4. Spectral decay of window functions $\tilde{\psi}_a^*(ak_\rho)$, $a = 1$ of order $m = 1, 3, 5, 7$.

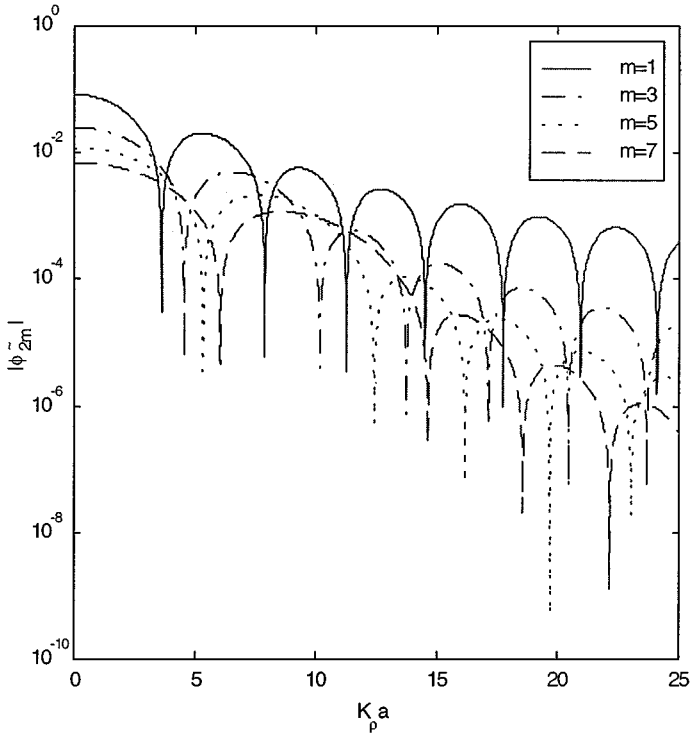

FIG. 5. Spectral decay of window functions $\tilde{\psi}_a^{**}(ak_\rho)$, $a = 1$ of order $m = 1, 3, 5, 7$.

where for positive or zero integers μ, ν

$$I_\mu^\nu(z) = \int_0^z \rho^\mu J_\upsilon(\rho)\, d\rho.$$

For small arguments of $z = ak_\rho$, $I_\mu^\nu(z)$ and (4.15)–(4.17) can be calculated directly with Gaussian quadrature, while for large values of z, we can use the formulas

$$I_\mu^\nu(z) = 2^\mu \frac{\Gamma\left(\frac{\nu+\mu+1}{2}\right)}{\Gamma\left(\frac{\nu-\mu+1}{2}\right)} + z[(\mu+\nu-1)J_\nu(z)S_{\mu-1,\nu-1}(z) - J_{\nu-1}(z)S_{\mu,\nu}(z)],$$

where $S_{\mu,\nu}(z)$ are the Lommel functions (see Appendix A.2).

5. NUMERICAL RESULTS

In this section, we validate Algorithm 2 for the fast calculation of dyadic Green's functions in homogeneous and multilayered media. In all cases, the frequency in the Green's function $f = 1$ GHz.

5.1. *Window Functions in Spectral Domain*

The window function $\psi_a(x, y)$ of order m has a compact support in the physical domain while in the spectral domain it decays in an algebraic order $1/k_\rho^m$; so do both $\tilde{\psi}_a^*(k_\rho)$ and $\tilde{\psi}_a^{**}(k_\rho)$ used in Algorithm 2. Figure 3 shows both window functions $\psi_a(x, y)$ of order $m = 3, 5, 7$ with support size $a = 1$ (lower left insert) and their frequency decays,

respectively. Figures 4 and 5 show the frequency decays of $\tilde{\psi}_a^*(k_\rho)$ and $\tilde{\psi}_a^{**}(k_\rho)$ of order $m = 1, 3, 5, 7$ with support $a = 1$, respectively.

5.2. *Second-Order Accuracy and Efficiency of Algorithm 2*

Algorithm 2 is second-order accurate, $O(a^2)$. The contour integrations in the definition of $W_i(\rho)$, $i = 0, 1, 2$, of Algorithm 2 are only evaluated over a truncated finite path as in Fig. 2. By choosing the L_4 portion of contour C according to (4.22), we can maintain an overall error of $O(a^2)$. To verify the second-order accuracy, we apply Algorithm 2 to calculate the scalar potential for the free-space Green's function

$$G_v(\rho, z; z') = \frac{1}{4\pi} \frac{e^{-jkR}}{R}, \tag{5.1}$$

where $R = |\mathbf{r} - \mathbf{r}'|$.

Figure 6 shows the real and imaginary parts of calculated results for $G_v(\rho, z; z')$, $z = 0.001$ m, $z' = 0.002$ m. The lines are the exact solutions given by (5.1) and the symbols are the calculation by Algorithm 2 with $L_4 = 20/a$ in the contour of Fig. 2. A window $\psi_a(\rho)$ of order $m = 5$ and support size $a = 0.005$ m is used. Figure 7 shows the errors in log-scale of three applications of Algorithm 2 with three different window sizes $a = w, 2w$, and $4w$, where $w = 0.005$ m. It is clear to see that the convergence rate is $O(a^2)$.

Finally, Fig. 8 shows the savings of Algorithm 2 over the direct Sommerfeld integration of (4.4). In Fig. 8, G_f denotes the calculation results of Algorithm 2 (squares, diamonds,

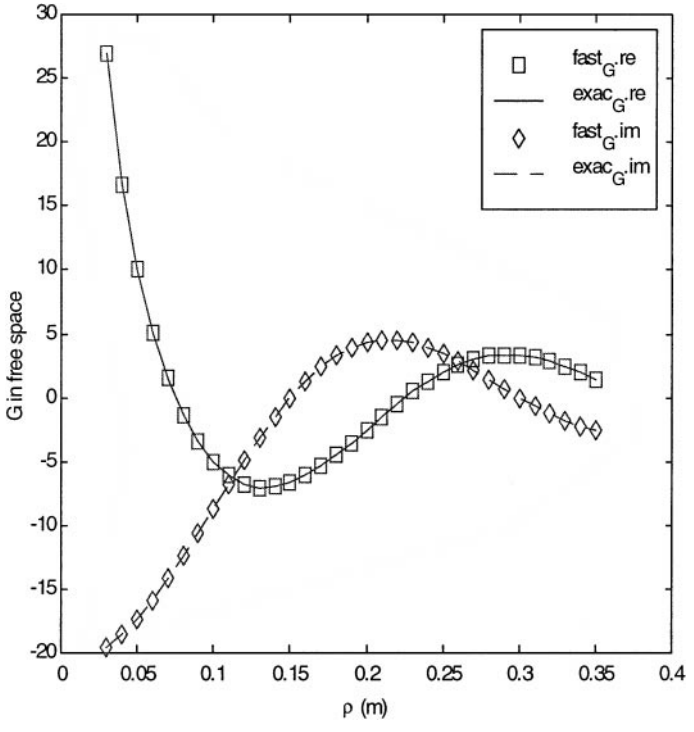

FIG. 6. Free-space scalar Green's function $G_V(\rho, z; z')$, $z = 0.001$ m, $z' = 0.002$ m. Lines indicate analytic results; symbols are for calculations with Algorithm 2 with window $\psi_a(\rho)$ of order $m = 5$ and window support $a = 0.005$ m.

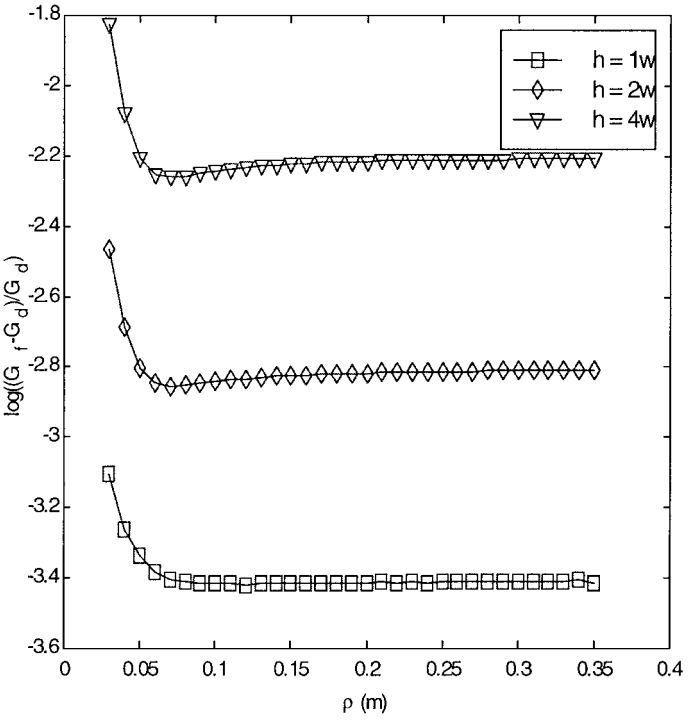

FIG. 7. Free-space scalar Green's function $G_V(\rho, z; z')$, $z = 0.001$ m, $z' = 0.002$ m. Relative errors with Algorithm 2 with window $\psi_a(\rho)$ of order $m = 5$ and window support $a = h,\ 2h$, and $4h$, where $h = 0.005$.

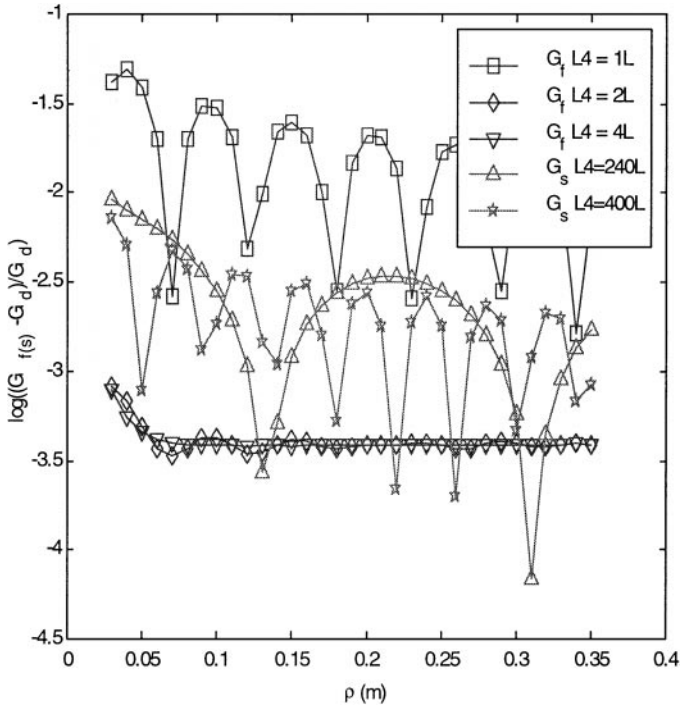

FIG. 8. Green's function $G_V(\rho, z; z')$, $z = 0.001$ m, $z' = 0.002$ m. Errors of Algorithm 2 with window function $\psi_a(\rho)$ of order $m = 5$ and $L_4 = L$, $2L(\diamondsuit)$, and $4L(\triangledown)$; $L = 5/a$; window support size $a = 0.005$. Errors of direct numerical integration of (4.4) using $L_4 = 240L(\triangle)$, $400L(\star)$.

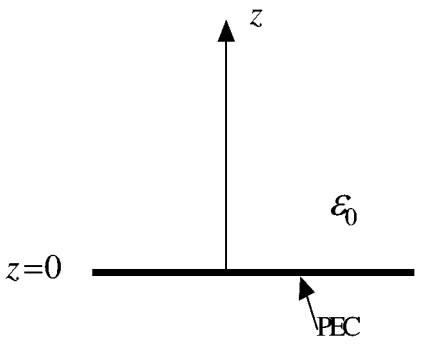

FIG. 9. Half free space over a PEC at $z = 0$.

down triangles) with the last portion of contour (2) $L_4 = L, 2L$, and $4L$, where $L = 5/a$ and $a = 0.005$ m is the support size of the window function of order $m = 5$. G_s denotes the direct integration of Sommerfeld integration (4.4), and upper triangles and stars are the results with a truncated contour $L_4 = 240L, 400L$, respectively. From Fig. 8, we can see that results of Algorithm 2 with $L_4 = 2L$ are already better than those of the direct Sommerfeld integration with $L_4 = 400L$; thus the contours used in Algorithm 2 are 200 times shorter than those used in direct integrations (4.4).

5.3. *Green's Functions for a Half Space over a PEC Ground Plane*

In this test case, we calculate the vector potential Green's function $G_A(\rho, z; z')$ for a half free space over a perfect conductor (PEC) ground plane at $z = 0$ in Fig. 9, where analytic forms of the Green's functions are available by using mirror images [11].

Figure 10 contains the calculated real and imaginary part of the scalar potential Green's function $G_V(\rho, z; z')$, $z = 0.001$ m, $z' = 0.002$ m. Again, window $\psi_a(\rho)$ of order $m = 5$ with support size $a = 0.005$ m is used and $L_4 = 20/a$ in the contour C of Fig. 2.

5.4. $\bar{G}_A(\rho, z; z')$, $G_V(\rho, z; z')$ *for a Five-Layered Medium*

In this test case, we calculate the dyadic Green's functions $\bar{G}_A(\rho, z; z')$, $G_V(\rho, z; z')$ for the five-layered medium depicted in Fig. 11. Four dielectric layers are used between the open air and a PEC ground plane. The relative dielectric constants for the four dielectric layers are, from top to bottom, $\epsilon_1 = 9.6$, $\epsilon_2 = 12.5$, $\epsilon_1 = 2.4$, and $\epsilon_1 = 3.6$, respectively. Their corresponding thickness are $h_1 = 0.001$ m, $h_2 = 0.003$ m, $h_1 = 0.002$ m, and $h_1 = 0.0015$ m, respectively.

Window $\psi_a(\rho)$ of order $m = 5$ with support size $a = 0.001$ m is used in Algorithm 2 and the $L_4 = 20/a$ is the last portion of the contour C in Fig. 2. Figure 12 shows the magnitude and imaginary and real parts (top to bottom, lines are from integration of Hankel transform (4.4); symbols are results of Algorithm 2) of the scalar Green's function $G_V(\rho, z; z')$ with $z = -0.0035$ m, $z' = -0.0062$ m. Figure 13 shows the component $G_A^{xx}(\rho, z; z')$ for the vector potential A along with the magnitude and imaginary and real parts of this component (top to bottom, lines are from integration of Hankel transform (4.4); symbols are results from Algorithm 2). Figure 14 shows similar results for the component $G_A^{zz}(\rho, z; z')$.

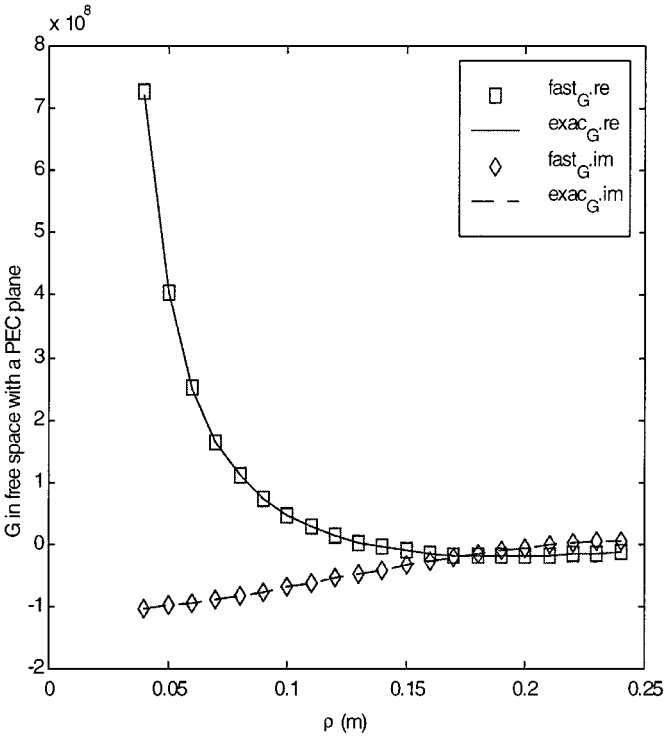

FIG. 10. $G_V(\rho, z; z')$, $z = 0.001$ m, $z' = 0.002$ m for a half free space over a PEC ground plane at $z = 0$. Lines are the analytic results; symbols are the results of Algorithm 2 with window $\psi_a(\rho)$ of order $m = 5$ and support size $a = 0.005$ m, with $L_4 = 20/a$ in the contour C of Fig. 2.

5.5. *Comparison with Method of Complex Images*

In the last numerical test, we compare our method with the method of complex images of [5, 6]. The method of complex images has been extensively used in the engineering communities for the calculation of dyadic Green's functions. The idea is based on the Sommerfeld identity

$$\frac{e^{-jkr}}{r} = -\frac{j}{2}\int_C dk_\rho H_0^{(2)}(k_\rho \rho)\frac{e^{-jk_z|z|}}{k_z}, \tag{5.2}$$

where $k_z = \sqrt{k^2 - k_\rho^2}$ and C is an integration contour from $-\infty$ to ∞ in the first and third quadrant of the complex k_ρ-plane.

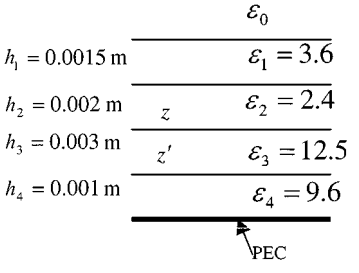

FIG. 11. A five-layer medium: four dielectrics layered between the air ($z = 0$) and a PEC ground plane.

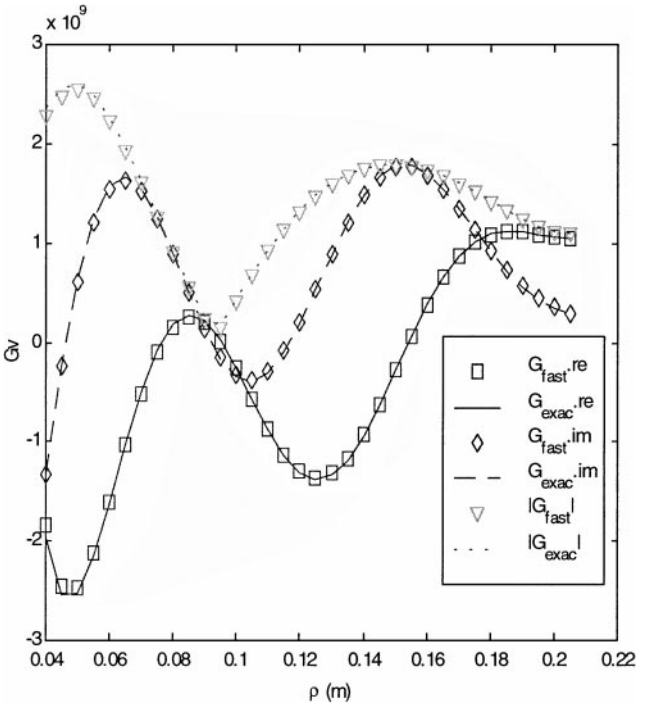

FIG. 12. Scalar Green's functions $G_V(\rho, z; z')$, $z = -0.0035$ m, $z' = -0.0062$ m for the five-layered medium in Fig. 9. Lines are results of direct integration of (4.4) for comparison; symbols are results of Algorithm 2 with window $\psi_a(\rho)$ of order $m = 5$ and window size $a = 0.001$ m, with $L_4 = 20/a$ in the contour C of Fig. 2.

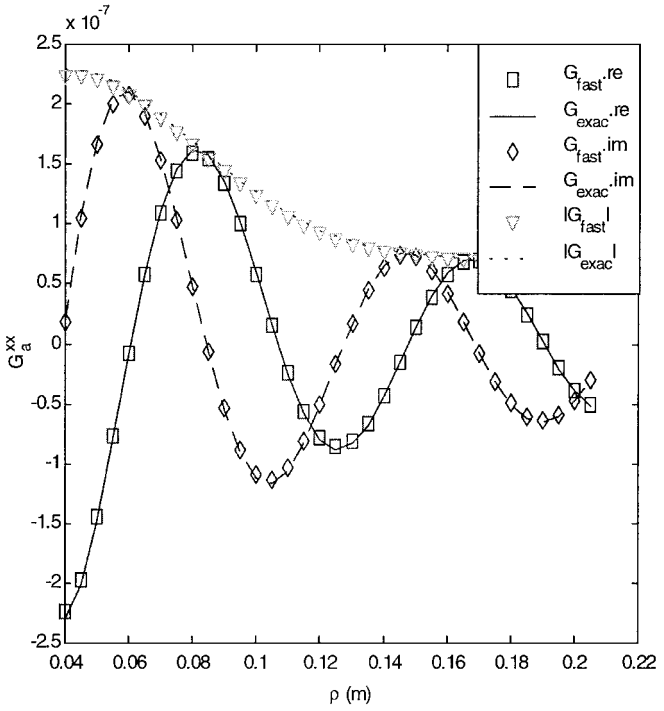

FIG. 13. Vector potential Green's functions $G_A^{xx}(\rho, z; z')$, $z = -0.0035$ m, $z' = -0.0062$ m for the five-layered medium in Fig. 9. Lines are results of direct integration of (4.4) for comparison; symbols are results of Algorithm 2 with window $\psi_a(\rho)$ of order $m = 5$ and window size $a = 0.001$ m, with $L_4 = 20/a$ in the contour C with Fig. 2.

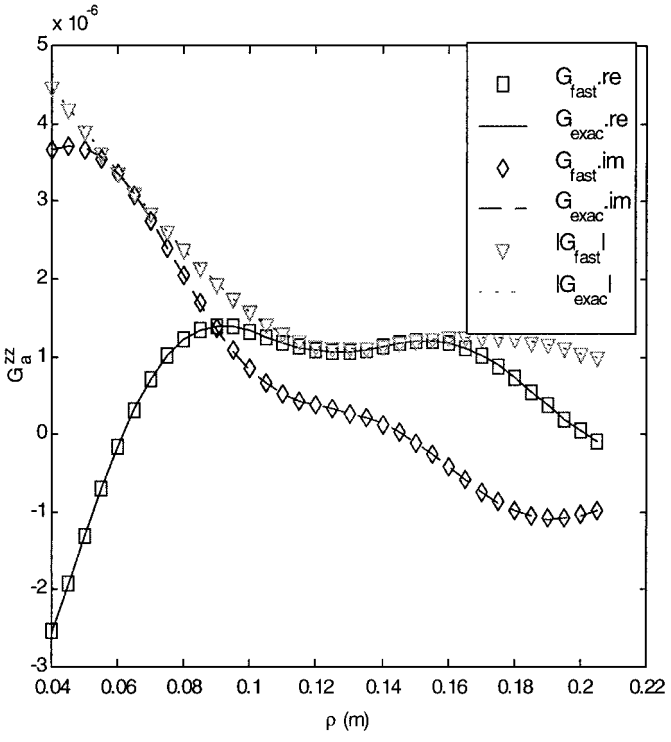

FIG. 14. Vector potential Green's functions $G_A^{zz}(\rho, z; z')$, $z = -0.0035$ m, $z' = -0.0062$ m for the five-layered medium in Fig. 9. Lines are results of direct integration of (4.4) for comparison; symbols are results of Algorithm 2 with window $\psi_a(\rho)$ of order $m = 5$ and window size $a = 0.001$ m, with $L_4 = 20/a$ in the contour C of Fig. 2.

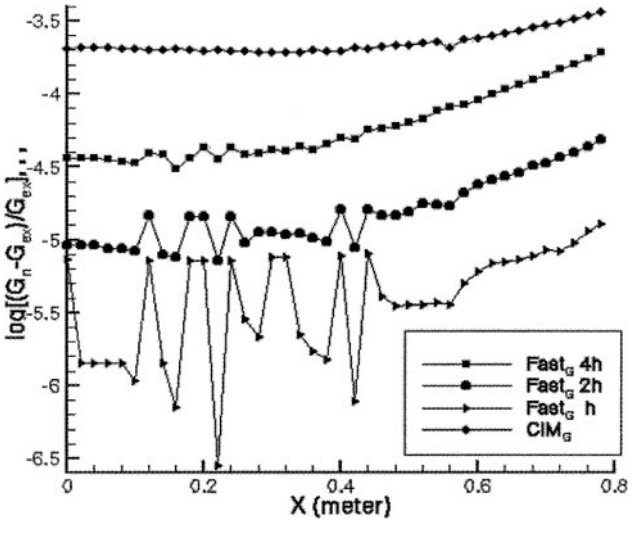

FIG. 15. Error comparison of the method of complex images (top line with 10 complex images) and our window-based fast algorithm (bottom three lines with window order $m = 5$ and support $a = 4h, 2h, h$ respectively, where $h = 0.001$ and $L_4 = 10/a$).

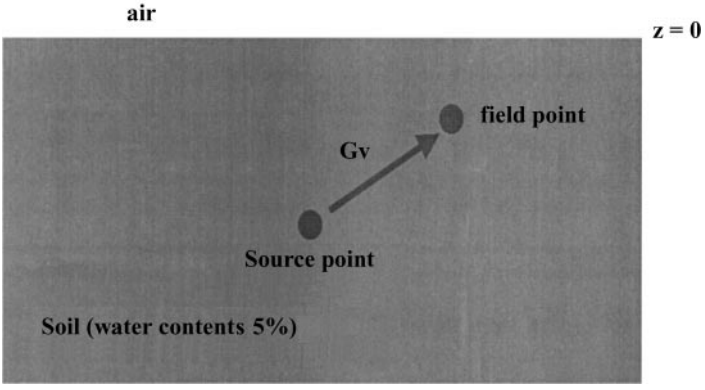

FIG. 16. Half space (air–soil with 5% water content).

The Green's function in the spectral domain is approximated by a sum of exponential functions, namely

$$\tilde{G}(k_\rho, z; z') \simeq \sum_{i=1}^{n} a_i \frac{e^{-jkr_i}}{r_i}, \tag{5.3}$$

where a_i is the complex magnitude and $r_i = \sqrt{\rho^2 + (z + z' - jb_i)^2}$ is the complex distance of the complex images. The coefficients a_i and b_i are obtained using a Prony method to fit sampled values of the $\tilde{G}(k_\rho)$ along a finite portion of the integration path C.

We have found out that such an approach will give good results when the source and observation points are on the same layer of a multilayered structure. However, the method of complex images does not perform well when source and observation points are not on the same level, and the Prony procedure for obtaining the coefficients a_i and b_i also becomes unstable and inefficient when high-frequency problems are considered.

In Figure 15, we present the results of both the method of complex images and our method (with $m = 5$ and $L_4 = 10/a$ and three different values of $a = 4h$, $2h$, and h, with $h = 0.001$) for the two-layer structure of Fig. 16 (air over soil with 5% water content). The top line is the relative error in logrithmic scale with complex images (10 complex images); the other three lines depict the relative error in logrithmic scale with decreaing size of a.

6. CONCLUSION

We have proposed a novel acceleration method for calculation of the Sommerfeld integrals in the definition of dyadic Green's functions for electromagnetic scattering of conductors embedded in multilayered media. The introduction of a window function effectively reduces the cost of the calculation of the Sommerfeld integration by forcing a faster decay of the integrands. The efficiency and accuracy of the calculation of the multilayered Green's functions are critical to the speed of the method of moments for the electromagnetic scattering of conductors in multilayered media. Numerical results presented in this paper and also in [10] show the effectiveness and accuracy of the proposed method. Because Algorithm 2 involves three integrals, compared with just one in Algorithm 1, a combination of the two algorithms can give better efficiency. Moreover, the fast Hankel transformation approach

proposed in [17] can be combined with Algorithms 1 and 2 for further speeding up of the calculation.

APPENDIX

A.1. *Proof of Lemma 3 (4.12)*

From the definition of the convolution, we have with $\Delta z = z - z'$

$$\begin{aligned} & G_2(\rho, z; z') * \psi_a(x, y) \\ & = \frac{1}{2\pi} \int_{-\infty}^{\infty} \int_{-\infty}^{\infty} (x'^2 + y'^2 + \Delta z^2) G(x', y', z; z') \psi_a(x - x', y - y')\, dx' dy' \\ & = r^2 [G(\rho, z; z') * \psi_a(x, y)] - 2x[G(\rho, z; z') * x\psi_a(x, y)] \\ & \quad - 2y[G(\rho, z; z') * y\psi_a(x, y)] + G(\rho, z; z') * ((x^2 + y^2)\psi_a(x, y)) \\ & = r^2 W_0(\rho) - 2x V_1 - 2y V_2 + W_2(\rho). \end{aligned} \tag{A.1}$$

In arriving at the second equation, we have used identities $x'^2 = x^2 + 2x(x' - x) + (x' - x)^2$ and $y'^2 = y^2 + 2y(y' - y) + (y' - y)^2$. Using the integral definition of the Bessel function,

$$J_n(z) = \frac{j^{-n}}{\pi} \int_0^{\pi} e^{jz\cos\theta} \cos n\theta\, d\theta,$$

we can show that

$$V_1 = G(\rho, z; z') * x\psi_a(x, y) = \cos\theta \int_0^{\infty} \tilde{G}(k_\rho, z; z') J_1(\rho k_\rho) \tilde{\psi}_a^*(k_\rho)\, k_\rho\, dk_\rho \tag{A.2}$$

and

$$V_2 = G(\rho, z; z') * y\psi_a(x, y) = \sin\theta \int_0^{\infty} \tilde{G}(k_\rho, z; z') J_1(\rho k_\rho) \tilde{\psi}_a^*(k_\rho)\, k_\rho\, dk_\rho, \tag{A.3}$$

where $\tilde{\psi}_a^*(k_\rho)$ is defined in (4.16). Therefore,

$$\begin{aligned} x V_1 + y V_2 &= \rho \int_0^{\infty} \tilde{G}(k_\rho, z; z') J_1(\rho k_\rho) \tilde{\psi}_a^*(k_\rho)\, k_\rho\, dk_\rho \\ &= \rho S_0[\tilde{G}(k_\rho, z; z') \tilde{\psi}_a^*(k_\rho)](\rho) = \rho W_1(\rho). \end{aligned} \tag{A.4}$$

Similarly, we can show that

$$W_2(\rho) = G(\rho, z; z') * ((x^2 + y^2)\psi_a(x, y)) = S_0[\tilde{G}(k_\rho, z; z') \tilde{\psi}_a^{**}(k_\rho)](\rho), \tag{A.5}$$

where $\tilde{\psi}_a^{**}(k_\rho)$ is given in (4.17). Substituting (A.4) and (A.5) into (A.1), we have the proof of (4.12).

A.2. *Lommel Function*

If $\mu + \nu$ or $\mu - \nu$ is a positive integer, then $S_{\mu,\nu}(z)$ has a finite polynomial expansion in terms of $1/z$, i.e.,

$$S_{\mu,\nu}(z) = z^{\mu-1} \sum_{k=0}^{n} \frac{\Gamma(-ia+1)\Gamma(-ib+1)}{\Gamma(-ia-k+1)\Gamma(-ib-k+1)} (-1)^k \left(\frac{2}{z}\right)^{2k}$$

with $n = \min(-ia, -ib)$, $ia = \frac{1-\mu+\nu}{2}$, $ib = \frac{1-\mu-\nu}{2}$.

For other values of μ, ν, we have the asymptotic approximations [19]

$$\begin{aligned} S_{\mu,\nu}(z) &\approx z^{\mu-1} {}_3F_0\left(1, ia, ib, -\frac{4}{z^2}\right) \\ &= z^{\mu-1}\left\{1 - \frac{(\mu-1)^2 - \nu^2}{z^2} + \frac{[(\mu-1)^2 - \nu^2][(\mu-3)^2 - \nu^2]}{z^4} \right. \\ &\quad \left. - \frac{[(\mu-1)^2 - \nu^2][(\mu-3)^2 - \nu^2][(\mu-5)^2 - \nu^2]}{z^6} + \cdots \right\}, \end{aligned}$$

where ${}_3F_0(1, ia, ib, -\frac{4}{z^2})$ is the hypergeometric function [19].

ACKNOWLEDGMENTS

The authors acknowledge the support of DARPA with a grant AFOSR F49620-96-1-0341 and NSF grant CCR–9972251 for the work reported in this paper. Thanks are extended to Professor Jiayuan Fang and Dr. Xingchao Yuan for many interesting discussions.

REFERENCES

1. K. Nabors and J. White, Fastcap: A multipole accelerated 3-D capacitance extraction program, *IEEE Trans. Computer-Aided Design of Integrated Circuits Syst.* **10**, 1447 (1991).
2. R. F. Harrington, *Field Computation by Moment Methods* (Macmillian, New York, 1968).
3. J. R. Mosig, Integral equation technique, in *Numerical Techniques for Microwave and Millimeter-Wave Passive Structure*, edited by T. Itoh (Wiley, New York, 1989), p. 133.
4. K. Michalski and J. R. Mosig, Multilayered media Green's functions in the integral equation formulations, *IEEE Trans. Antennas Propag.* **AP-35**(11), 1299 (1987).
5. Y. L. Chow, J. J. Yang, D. G. Fang, and G. E. Howard, A closed form spatial Green's function for the thick microstrip substrate, *IEEE Trans. Microwave Theory Tech.* **39**, 588 (1991).
6. M. I. Aksun, A robust approach for the derivation of closed-form Green's functions, *IEEE Trans. Microwave Theory Tech.* **44**, 651 (1996).
7. T. J. Cui and W. C. Chew, *Fast Evaluation of Sommerfeld Integrals for EM Scattering and Radiation by Three Dimensional Buried Objects*, Research Report No. CCEM-34-97, University of Illinois, Urbana, IL, 1997.
8. I. Daubechies, *Ten Lectures on Wavelets*, CBMS Series 61 (SIAM, Philadephia, 1992).
9. D. Gottlieb and E. Tadmor, Recovering pointwise values of discontinuous data within spectral accuracy, in *Progress and Supercomputing in Computational Fluid Dynamics*, edited by E. M. Murman and S. S. Arbarbanel (Birkhauser, Boston, 1985), p. 357.
10. W. Cai and T. Y. Yu, High order mixed RWG basis functions for electromagnetic scattering and applications. Submitted for publication.
11. J. A. Stratton, *Electromagnetic Theory* (McGraw-Hill, New York, 1941).
12. A. Sommerfeld, *Partial Differential Equations in Physics* (Academic Press, New York, 1964).

13. A. Erteza and B. K. Park, Nonuniqueness of resolution of Hertz vector in presence of a boundary, and the horizontal problem, *IEEE Trans. Antennas Propag*. **AP-17**, 376 (1969).
14. K. A. Michalski, On the scalar potential of a point charge associated with a time-harmonic dipole in a layered medium, *IEEE Trans. Antennas Propag.* **AP-35**(11), 1299 (1987).
15. C. H. Wilcox, Debye potentials, *J. Math. Mech.* **6**, 167 (1957).
16. J. Van Bladel, *Singular Electromagnetic Fields and Sources* (IEEE Press, New York, 1991).
17. S. Kapur and V. Rokhlin, *An Algorithm for the Fast Hankel Transform*, Technical Report 1045, Computer Science Department, Yale University, 1995.
18. K. A. Michalski and D. Zheng, Electromagnetic scattering and radiation by surfaces of arbitrary shape in layered media, Part I: Theory, *IEEE Trans. Antennas Propag.* **AP-45**, 508 (1997).
19. H. Batman, *Higher Transcendental Functions* (McGraw-Hill, New York, 1953), Vols. I, II.